



**HAL**  
open science

## Frictional Anisotropy of 3D-Printed Fault Surfaces

Tom Vincent-Dospital, Alain Steyer, François Renard, Renaud Toussaint

► **To cite this version:**

Tom Vincent-Dospital, Alain Steyer, François Renard, Renaud Toussaint. Frictional Anisotropy of 3D-Printed Fault Surfaces. *Frontiers in Earth Science*, 2021, 9, pp.627823. 10.3389/feart.2021.627823 . hal-03547333

**HAL Id: hal-03547333**

**<https://hal.science/hal-03547333>**

Submitted on 28 Jan 2022

**HAL** is a multi-disciplinary open access archive for the deposit and dissemination of scientific research documents, whether they are published or not. The documents may come from teaching and research institutions in France or abroad, or from public or private research centers.

L'archive ouverte pluridisciplinaire **HAL**, est destinée au dépôt et à la diffusion de documents scientifiques de niveau recherche, publiés ou non, émanant des établissements d'enseignement et de recherche français ou étrangers, des laboratoires publics ou privés.



# Frictional Anisotropy of 3D-Printed Fault Surfaces

Tom Vincent-Dospital<sup>1,2\*</sup>, Alain Steyer<sup>1</sup>, François Renard<sup>3,4</sup> and Renaud Toussaint<sup>1,2\*</sup>

<sup>1</sup>Université de Strasbourg, ITES UMR 7063, Strasbourg, France, <sup>2</sup>SFF Porelab, The Njord Centre, Department of Physics, University of Oslo, Oslo, Norway, <sup>3</sup>The Njord Centre, Department of Geosciences, University of Oslo, Oslo, Norway, <sup>4</sup>Université Grenoble Alpes, Université Savoie Mont Blanc, CNRS, IRD, IFTTAR, ISTerre, Grenoble, France

The surface morphology of faults controls the spatial anisotropy of their frictional properties and hence their mechanical stability. Such anisotropy is only rarely studied in seismology models of fault slip, although it might be paramount to understand the seismic rupture in particular areas, notably where slip occurs in a direction different from that of the main striations of the fault. To quantify how the anisotropy of fault surfaces affects the friction coefficient during sliding, we sheared synthetic fault planes made of plaster of Paris. These fault planes were produced by 3D-printing real striated fault surfaces whose 3D roughness was measured in the field at spatial scales from millimeters to meters. Here, we show how the 3D-printing technology can help for the study of frictional slip. The results show that fault anisotropy controls the coefficient of static friction, with  $\mu_{S//}$ , the friction coefficient along the striations being three to four times smaller than  $\mu_{S\perp}$ , the friction coefficient along the orientation perpendicular to the striations. This is true both at the meter and the millimeter scales. The anisotropy in friction and the average coefficient of static friction are also shown to decrease with the normal stress applied to the faults, as a result of the increased surface wear under increased loading.

**Keywords:** friction, anisotropy, seismic faults, 3D printing, plaster 3D model, frictional damages

## OPEN ACCESS

### Edited by:

Takashi Nakagawa,  
Kobe University, Japan

### Reviewed by:

Shengji Wei,  
Nanyang Technological University,  
Singapore  
Amir Sagy,  
Geological Survey of Israel, Israel

### \*Correspondence:

Tom Vincent-Dospital  
tom.vincent-dospital@fys.uio.no  
Renaud Toussaint  
renaud.toussaint@unistra.fr

### Specialty section:

This article was submitted to  
Solid Earth Geophysics,  
a section of the journal  
Frontiers in Earth Science

**Received:** 10 November 2020

**Accepted:** 05 January 2021

**Published:** 07 May 2021

### Citation:

Vincent-Dospital T, Steyer A, Renard F  
and Toussaint R (2021) Frictional  
Anisotropy of 3D-Printed  
Fault Surfaces.  
Front. Earth Sci. 9:627823.  
doi: 10.3389/feart.2021.627823

## 1 INTRODUCTION

Faults in the Earth's crust are complex systems along which earthquakes nucleate and propagate [e.g., Wibberley et al. (2008)]. Faults hold structures and heterogeneities at all scales [Brown and Scholz (1985), Renard et al. (2006), Candela et al. (2012)]. While they are often simplified to their simplest two-dimensional description (i.e., the fault plane), increasing complexity is now added to faults models [e.g., Rice and Ben-Zion (1996)]. It is indeed considered that, to fully understand seismicity in various areas, it is paramount to account for some disorder in the faults frictional properties such as secondary faulting, off-fault damage or roughness of the fault plane [Pechmann and Kanamori (1982), Aochi and Ide (2009), Candela et al. (2011), Ando et al. (2012), Tesei et al. (2014), Allam et al. (2019), Bruhat et al. (2019), Sagy and Lyakhovskiy (2019)]. For instance, the volume of damaged rocks, during the activation of a fault, depends on the initial contact roughness [Queener et al. (1965)] and, thus, a fault with a stronger roughness presents a different energy budget than a flat fault, as more energy is converted into surface area energy. In particular, roughness encourages the triggering of local events, but is believed to prevent the propagation of large-slip earthquakes [Bruhat et al. (2019)]. Additionally, large scale roughness tends to inhibit the propagation of any rupture faster than the shear wave velocity of surrounding rocks [Bouchon et al. (2010)].

Another degree of complexity is more rarely considered when modeling geological contacts and fault slip; the possible anisotropy in their frictional properties. Morphological anisotropy is a known

feature of faults, notably impacting the seismic waves velocity in their vicinity [Evans (1984), Cochran et al. (2003); Li et al. (2015)] or the mobility of natural and injected fluids [Vadacca et al. (2018)] in the subsurface. Frictional anisotropy, interestingly, is also regularly studied in other fields than seismology, for instance the tribology of rubber tires [Carbone et al. (2009), Tiwari et al. (2016)], the strength of advanced adhesives Jin et al. (2012), or the mitigation of water condensation Pionnier et al. (2018). It is also considered to play a major role in nature Filippov and Gorb (2013), for instance in the motion of numerous animals [Zheng et al. (2007), Jin et al. (2012), Filippov et al. (2018)] and the hydration of some plants [Roth-Nebelsick et al. (2012), Wang F. et al. (2017)]. In most cases, frictional anisotropy derives from the existence of preferential topographical orientations on, at least, one of the contact surfaces [Yu and Wang (2012), Tapia et al. (2016)]. The length scale for such structural directivity can be as small as micrometer [Stupkiewicz et al. (2014)] to nanometer [Fessler et al. (2019), Gong et al. (2018)].

In seismic faults, such preferential orientations in their topography are observed at all scales [Renard et al. (2006), Candela et al. (2012), Brown and Scholz (1985)] and originate from several processes. At the molecular level, rock forming crystals may display some frictional anisotropy. It is notably the case for antigorite, a mineral abundant in the Earth's upper mantle [Campione and Capitani (2013)]. At the mesoscopic scale, the shear strength of foliated rocks is known to be anisotropic, due to the oriented planes in their constitutive mineralogy [Shea and Kronenberg (1993), Rawling et al. (2002)]. Fault zones in sedimentary basins are initiated by early fractures that often propagate in layered sediments. It can result in an anisotropic ramp-flat morphology of these fracture surfaces [Peacock and Sanderson (1992)]. For more mature faults having accumulated enough displacement, and above a given length scale [Candela and Brodsky (2016)], the topography of the fault planes is also marked by slip induced wear, with striations and grooves of various wavelengths and amplitudes oriented along the main direction of slip [Engelder (1974); Edwards et al. (2018)]. If such morphological anisotropy of fault surfaces is well-known, its effect on the anisotropy of the frictional properties remains to be characterized. Such a characterization of frictional anisotropy could also be of interest for other types of rock contacts than strictly seismic faults, in particular for shallow rock joints and fractures, whose three-dimensional geometry is key in geotechnical engineering and for the structural stability of many man-made constructions [Barton and Choubey (1977), Seidel and Haberfield (1995), Grasselli and Egger (2003), Li et al. (2020)]. Here, we study how the morphology of faults controls the static coefficient of friction and the anisotropy of friction with regards to the main stress orientation during slip. To reach this goal, we produce 3D-prints of actual faults surfaces whose topography was measured in the field [Candela and Renard (2012)]. We perform friction experiments with plaster of Paris casts of these 3D-printed faults. Results show that the coefficient of static friction along faults is highly anisotropic, a property that should henceforward be considered in numerical models of slip on seismic faults. We also show that this anisotropy is stress-dependent and should decrease with depth [e.g., Byerlee (1978)].

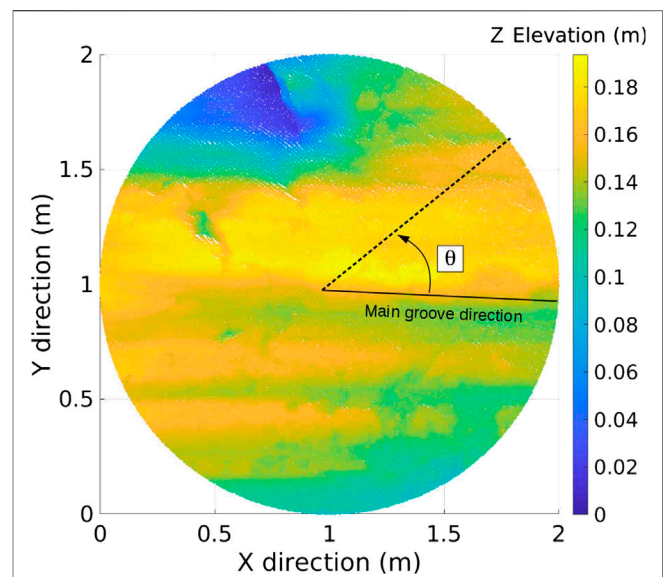


**FIGURE 1** | Topography (i.e., roughness) of the Corona Heights fault at the meter scale [Candela and Renard (2012), Renard (2020)]. This surface, called  $S_m$ , has a radius of 1 m and is defined on a 5 mm grid with a 1.25 mm elevation resolution. A parametric angle  $\theta$  is defined from the main groove orientation.

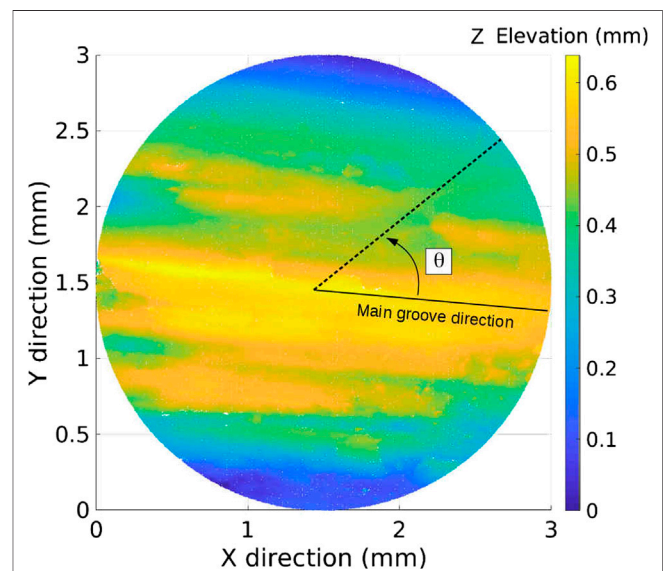


**FIGURE 2** | White light interferometry measurement of the topography of the Corona Heights fault plane at the millimeter scale [Candela and Renard (2012), Renard (2020)]. This surface, called  $S_{mm}$ , has a radius of 1.5 mm and is defined on a  $2\ \mu\text{m}$  grid with a  $0.025\ \mu\text{m}$  elevation resolution. A parametric angle  $\theta$  is defined from the main groove orientation.

## 2 3D PRINTING AND PLASTER CASTING OF FAULT PLANES

The actual morphology of natural faults can be difficult to assess, even if their long wavelength structures can be inferred by surface or subsurface imaging techniques [Massonnet et al. (1993), Blakely et al.

(2002), Edwards et al. (2018)]. Yet, some fault planes are accessible to direct high resolution measurements, notably as they were exhumed by erosion and tectonic processes. For this study, we have used a series of digital fault surfaces. These fault roughness data were acquired with Light Detection and Ranging (LiDAR), laboratory laser profilometry, or white light interferometry techniques [Candela et al. (2012)]. These data are available on an online public database [Candela and Renard (2012)] and in a repository with a DOI number [Renard (2020)]. Should the reader hold some similar data, these authors welcome additions to this database. We have specifically selected fault roughness measurements performed on the Corona Heights fault [Candela et al. (2011)] that outcrops near the Peixotto playground in San Francisco, California. These data cover surface areas with spatial scales in the range of millimeters to meters. **Figures 1, 2** show the fault surface at two spatial scales, one surface at the meter scale, defined on a 5 mm × 5 mm grid, and one surface at the millimeter scale, defined on a 2 μm × 2 μm grid. We will further refer to these two surfaces as, respectively,  $S_m$  and  $S_{mm}$ . Already, one can notice some preferential orientations in these topographies, and that the amplitude of fault roughness is, relatively to their size, somewhat larger at smaller scales ( $S_{mm}$ ) than at larger scales ( $S_m$ ) [Brodsky et al. (2016)].

For our tests, we chose to limit these anisotropic surfaces to a circular sample geometry. We also applied a mild running-window median filter to smooth out spikes in the measured surfaces that could be associated to measurement noise. The window length of the filter was 10 space steps, accounting for 5 cm for  $S_m$  and for 20 μm for  $S_{mm}$ . In order to run the friction experiments, we generated some opposing surfaces to the ones presented in **Figures 1, 2**. These opposing surfaces could not be measured, as the actual fault walls that were facing  $S_m$  and  $S_{mm}$  are now eroded. To reconstruct them, we have applied the following transformation to the 3D coordinates ( $X, Y, Z$ ) of  $S_m$  and  $S_{mm}$ :

$$\begin{aligned} X' &\sim X \\ Y' &\sim -Y \\ Z' &\sim -Z, \end{aligned} \tag{1}$$

where  $X'$ ,  $Y'$ , and  $Z'$  are the coordinates of the generated opposing surfaces and ( $X, Y$ ) give the map location of a given surface point of elevation  $Z$ , as represented in **Figure 1**. We have

thus assumed that the missing fault walls are complementary to the measured ones, so that, when pressed together before the friction tests, they form a bulk with negligible aperture between the two blocks. Such assumption for natural faults would only be partly verified. When having accumulated enough slip, a granular layer of gouge material may there have formed, and the two opposing sliding surfaces may not always perfectly match. However, our assumption is relevant for the youngest faults with a small amount of slip. We have also assumed that erosion did not significantly alter the fault plane, such that the measured topography is representative of the one of an actual buried fault. For the Corona Heights fault, this assumption is valid because the fault offsets silica-rich chert rocks with a high resistance to weathering.

After having obtained the surfaces, we isotropically (i.e., with the same factor in all directions) down- or up-scaled  $S_m$  and  $S_{mm}$  to fit a standard 4 cm diameter disk that matches the clamp size of our shear deformation apparatus. We also regrided the surfaces to match the lateral resolution of our 3D printer {Ultimaker<sup>2</sup> Extended+ (Ultimaker2 Extended+, 2015)} that has a nozzle size of 250 μm. The four surfaces (two fault surfaces and two opposing surfaces) were then 3D-printed into polylactic acid (PLA) material, as shown in **Figure 3**. It should be noted that, even when designed to be flat, printed objects can present a natural roughness [Quinsat et al. (2018)], at a scale however smaller than the grooves observed on the printed faults. These intrinsic imperfections shall be comparable to 60 μm, the elementary thickness of the PLA layers deposited by our 3D printer. In comparison, the 2D standard deviation of the elevation in our printed objects topography are 0.66 mm for  $S_m$  and 1.7 mm for  $S_{mm}$ . The maximal elevation of these objects is, respectively, 3.7 and 8.3 mm. We thus consider that the small scale roughness (~60 μm) from the printer's limit in resolution has a second order effect on the frictional properties of the surfaces.

Although we could have performed the friction experiments with the plastic pieces produced with the 3D printer, we have rather produced samples of plaster of Paris (gypsum) blocks molded from the plastic faults. Plaster is known to be a reasonable model of porous brittle materials [Vekinis et al. (1993)], and the

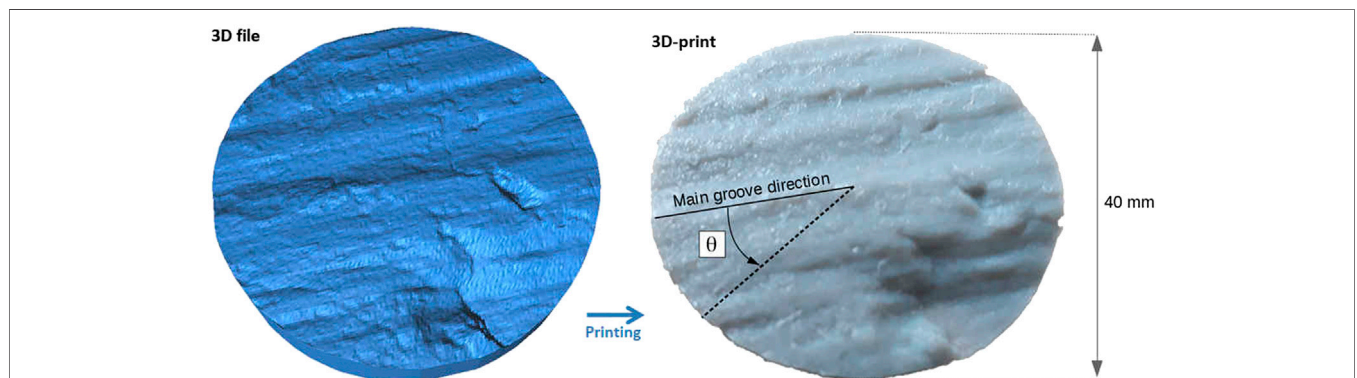


**FIGURE 3 | (Left)** 3D file (STL file) obtained from the measured topography of the  $S_m$  fault. The four 3D files generated for our friction experiments ( $S_m$ ,  $S_{mm}$ , and their respective complementary) are available as **Supplementary Material S1**. **(Right)** Picture of a Polylactic acid 3D-print of the  $S_m$  fault.



**FIGURE 4 |** Plaster faults made using the 3D-printed molds (i.e., an example of which is shown in **Figure 3**). **(Left)  $S_m$  (top)** and its complementary surface **(bottom)**. **(Right)  $S_{mm}$  (top)** and its complementary surface **(bottom)**. The samples have a diameter of 40 mm. One can appreciate that the fault at the millimeter scale ( $S_{mm}$ ) shows a higher roughness aspect than at the meter scale ( $S_m$ ).

main goal of these casts was to work with a rock-like material, notably because plaster may wear and deform differently than plastic under shear. The fragile nature of plaster, and the potential friction-induced wear that the plaster was subjected to in our experiments, made us use new casts for each experimental realization. The casts were generated with the following protocol: five volumes of water and eight volumes of powder of plaster of Paris were mixed and poured over the plastic molds, then let to dry during one and half hour. The molds, an example of which is shown in **Figure 3**, were sprayed before each cast with a thin layer of silicon grease to avoid some of the fine plaster details to stick to the plastic during the mold release. The last step in the casts preparation was to dry them in an oven at a temperature of 40°C for 1 h. As a result, we produced fault planes in blocks made of plaster of Paris, as shown in **Figure 4**.

### 3 EXPERIMENTAL SET-UP AND EXPERIMENTAL CONDITIONS

The shear apparatus used to perform the friction tests is shown in **Figure 5**. The two complementary surfaces are pressed together and mounted one on top of the other between the clamps of the shear apparatus. A normal force  $F_N$  is applied on the top surface by using adjustable weights. In addition, a spring system of stiffness 625 N m<sup>-1</sup> allows, if desired, to compensate for the machine empty weight of 13.7 N (i.e., the normal weight transmitted to the friction surfaces by the machine top clamp and structure and the top cast when

no extra mass is used). A tangential driving shear force  $F_T$  is then applied to the top fault wall in a given direction of the  $(X, Y)$  plane. The amplitude of the force is measured by a Sauter® force gauge (Sauter FH-S, 2018). The shear orientation is defined by the angle  $\theta \in [0^\circ \ 360^\circ]$  from the orientation of the main grooves on the fault surface, as defined in **Figures 1, 2**. A horizontal mechanical slider makes sure that the friction is evaluated in the direction of interest only, and a vertical slider allows upward or downward displacement of the top surface. While these sliders would ideally be perfectly lubricated, we have estimated their frictional resistance at the sliding velocity of our experiments,  $F_c = 4 \text{ N} \pm 0.5 \text{ N}$  by performing a friction test with no fault installed in the machine (that is, with only air between the two clamps represented in **Figure 5**).

The target speed of the test bench (that is, the demanded slip velocity) was fixed to a constant and equal to 1.3 mm s<sup>-1</sup>. Of course, such a velocity may be orders of magnitude above that of typical tectonic solicitations (for instance, an ultra-fast oceanic ridge may reach an opening rate of 10–20 cm yr<sup>-1</sup> [Renard et al. (1985)]). Here, we define the static friction in the experiments as the peak shear stress reached before sliding occurs divided by the normal stress.

We characterize the anisotropy of this laboratory static friction coefficient for both the  $S_m$  and  $S_{mm}$  surfaces by performing a series of experiments where we vary the angle of loading with respect to the grooves. We ran friction tests every 30° on both plaster faults. At each angle, the experiment was repeated at least three times in order to ensure that the results are reproducible (with new casts each time, to avoid any wear-related deviation). The standard deviation computed on these multiple measurements (typically 5–10 N) was used to compute the error bars on our characteristics coefficients of static friction.  $S_m$  was sheared under a normal stress  $\sigma_N = 10.9 \text{ kPa}$ , while the tests performed on the rougher surface  $S_{mm}$  were performed under  $\sigma_N = 26.5 \text{ kPa}$ . A total of 76 experiments were performed, 37 using  $S_m$  and 39 using  $S_{mm}$ . At the onset of slip, the laboratory static friction coefficient is defined using a standard Coulomb's law [Bowden and Tabor (1951)]:

$$\mu_s(F_N, \theta) = \frac{\max[F_T(F_N, \theta)] - F_c}{F_N}, \quad (2)$$

where  $\mu_s$  is the coefficient of static friction and  $\max[F_T]$  is the (local) maximum tangential force applied at the onset of slip. In the following, we will also consider the mean driving and normal stresses, denoted  $\sigma_T = F_T/(\pi r^2)$  and  $\sigma_N = F_N/(\pi r^2)$ , where  $r = 2 \text{ cm}$  is the radius of the cast. **Figure 6** shows a typical measurement of a friction test, from which  $\max[F_T]$  and hence  $\mu_s$  are calculated.

## 4 RESULTS

### 4.1 Friction Anisotropy

The results are presented in **Figure 7**. The derived coefficient of frictions are larger than 1, which does not come as a surprise due

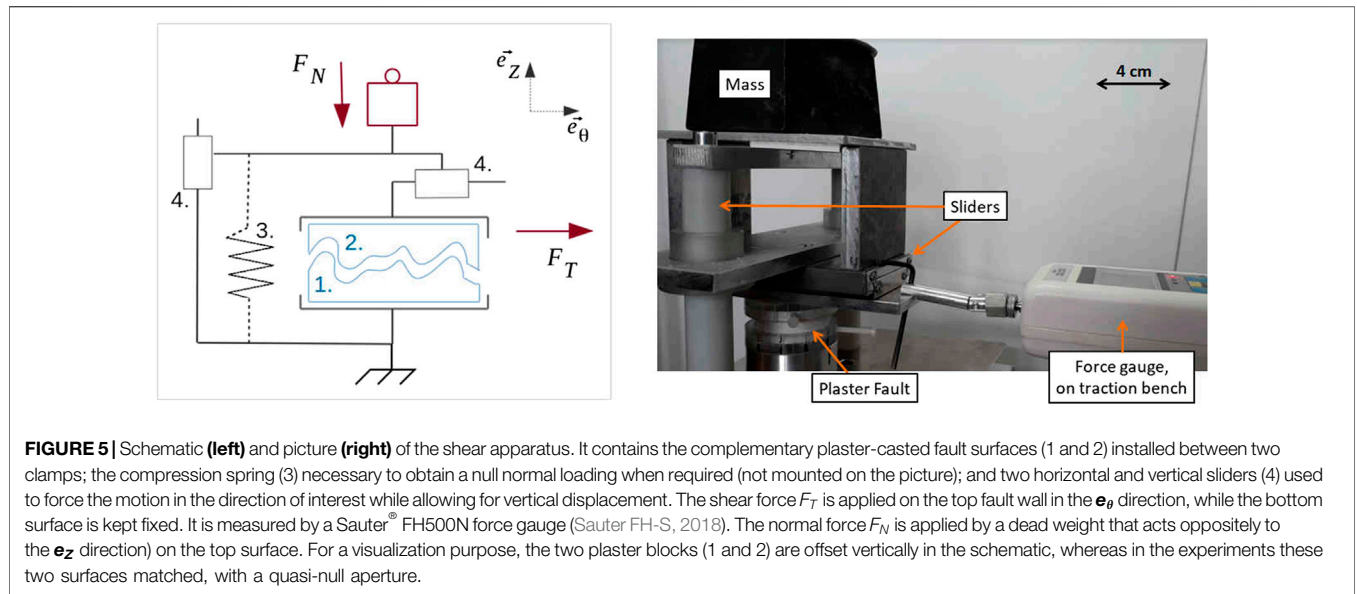


**FIGURE 5 |** Schematic (left) and picture (right) of the shear apparatus. It contains the complementary plaster-casted fault surfaces (1 and 2) installed between two clamps; the compression spring (3) necessary to obtain a null normal loading when required (not mounted on the picture); and two horizontal and vertical sliders (4) used to force the motion in the direction of interest while allowing for vertical displacement. The shear force  $F_T$  is applied on the top fault wall in the  $e_\theta$  direction, while the bottom surface is kept fixed. It is measured by a Sauter® FH500N force gauge (Sauter FH-S, 2018). The normal force  $F_N$  is applied by a dead weight that acts oppositely to the  $e_z$  direction on the top surface. For a visualization purpose, the two plaster blocks (1 and 2) are offset vertically in the schematic, whereas in the experiments these two surfaces matched, with a quasi-null aperture.

to the nonnegligible roughness of our fault samples. Indeed, a large part of the contact area is bound to be perpendicular to the demanded slip (in any direction), inducing a strong resistance to motion.

On both fault samples, one can observe the strong anisotropy of the coefficient of static friction, with the maximum value of  $\sigma_S$  being about four times larger than its minimum for  $S_m$  and about three times larger for  $S_{mm}$ . In both sets of experiments, the minimal friction is obtained along the main groove orientation (i.e., at  $\theta = 0^\circ$  or  $\theta = 180^\circ$ ), and the resistance to shear is larger perpendicularly to this orientation. The maximum of value is however never obtained exactly at  $\theta = 90^\circ$  or  $\theta = 270^\circ$  but rather along a neighboring direction. Local maxima are indeed obtained for  $\theta = 60^\circ$  or  $\theta = 240^\circ$  when shearing  $S_m$  and for  $\theta = 120^\circ$  or  $\theta = 300^\circ$  when shearing  $S_{mm}$ .

### 4.2 Damage and Stress Dependence

Most of our experiments were destructive, with visible wear on the plaster samples after the shearing tests. This wear was the main reason calling for the production of new plaster casts for each experimental realization, as we verified that repeating a same experiment with a previously used cast led to a significant (and here unwanted) drop in friction. The observed damage consists either in the formation of plaster powder (gouge) or in the rupture of topographic highs of the fault surfaces. Part of it might have initiated at the onset of the fault displacement (and hence be related to the static friction), while some of it has rather been induced by the subsequent sliding. Figure 8 shows some examples of these damage types.

Wear of seismic faults has been studied [e.g., Wang and Scholz (1994); Kim et al. (2004)] to, in particular, better understand the energy budget of the deformation, but also because this process may lubricate faults during slip [e.g., Rempel and Rice (2006), Di Toro et al. (2011)] or modify the fault permeability to fluid flow [e.g., Blanpied et al. (1992), Mitchell and Faulkner (2008)]. The present study focuses on the measurement of the coefficient of

static friction and on its anisotropy, but we suggest that our 3D-print-based set-up could also enable the quantitative characterization of damage during sliding along analog fault surfaces. We here keep to a qualitative assessment of which parts of the surfaces were mainly worn during each experiment. It seems that most of the shear resistance of the Corona Heights fault, at the millimeter scale ( $S_{mm}$ ), arises from its grooves. By contrast, the friction of  $S_m$  (representing a metric scale) is dominated by one chip in its field-scanned morphology (i.e., the main topographic low in Figure 1). This chip being on the edge of the 3D-printed surface, but not on the edge of the real world fault, a finite size effect (inducing an artificial asymmetry of the fault wall) is certainly at play in the results reported in Figure 7 (top), notably explaining the strong

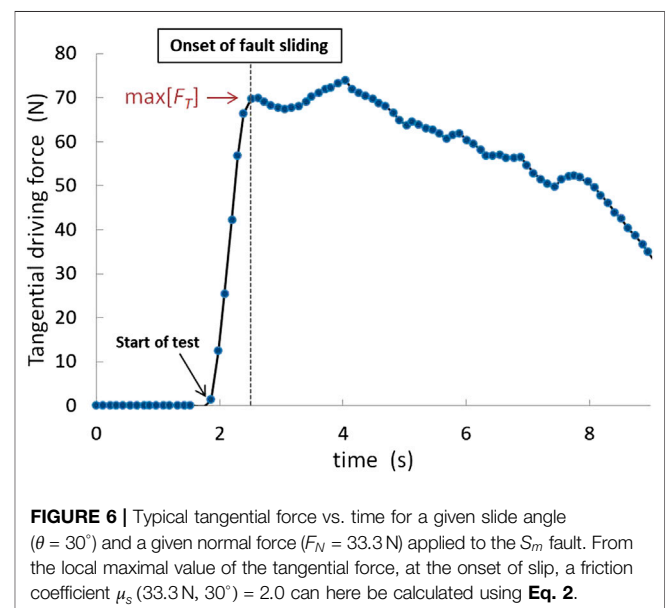
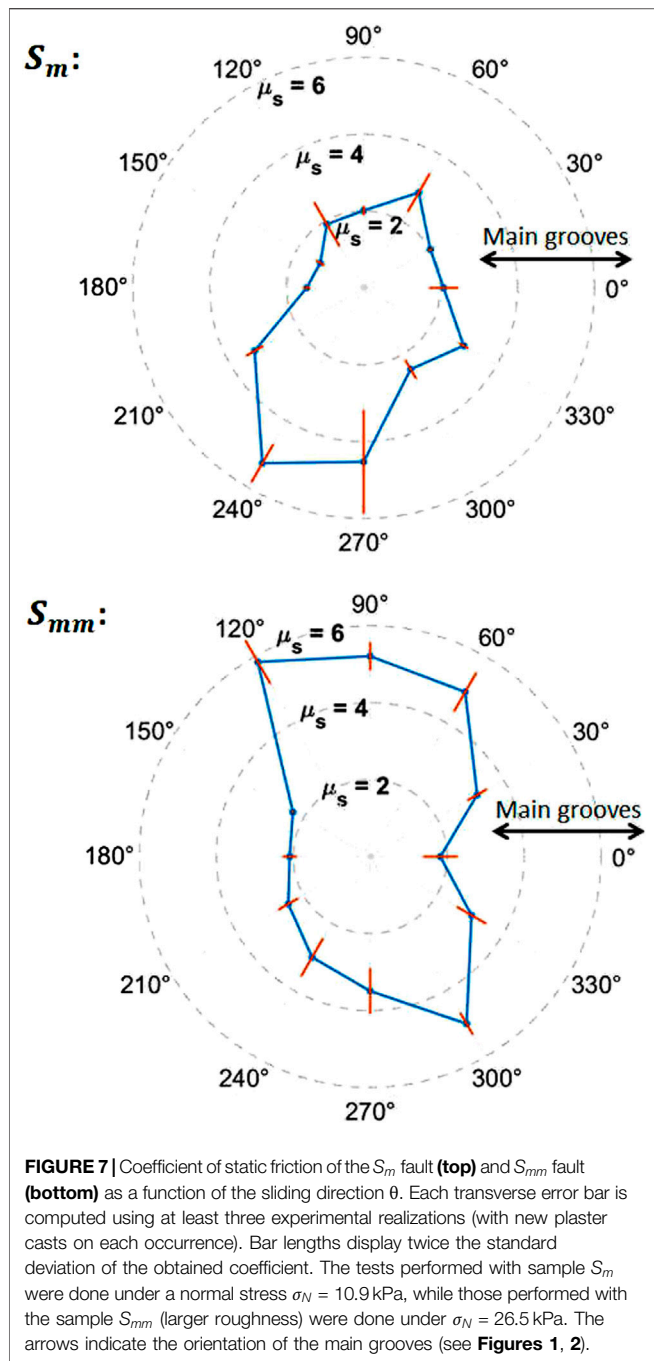
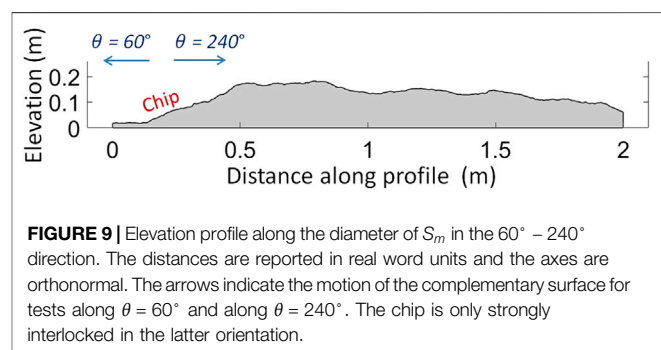
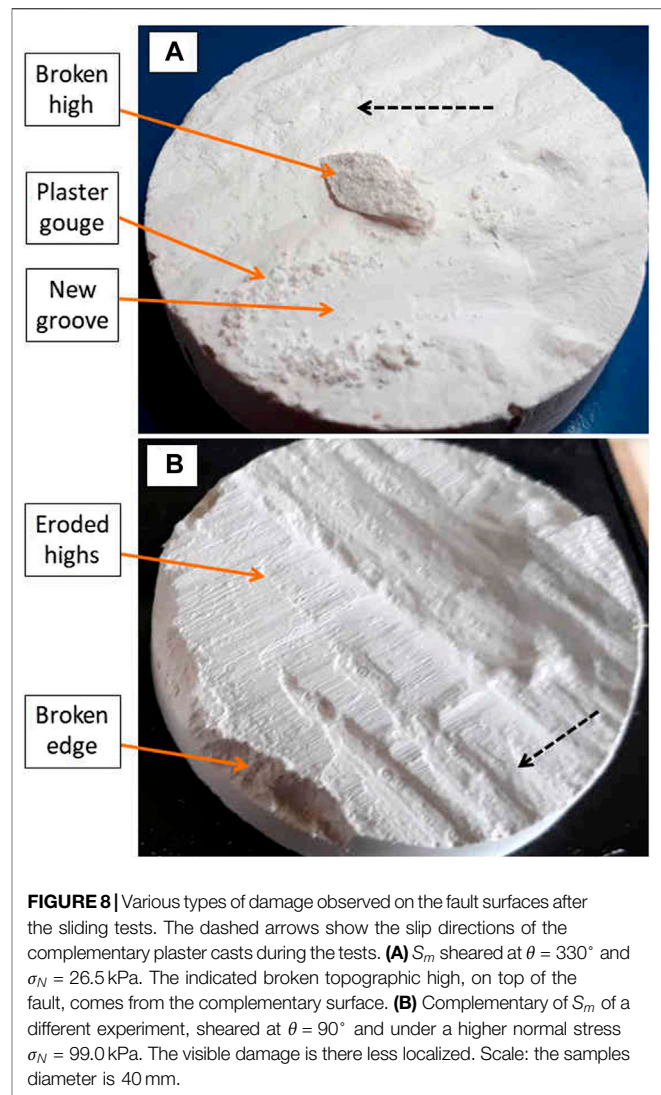


**FIGURE 6 |** Typical tangential force vs. time for a given slide angle ( $\theta = 30^\circ$ ) and a given normal force ( $F_N = 33.3$  N) applied to the  $S_m$  fault. From the local maximal value of the tangential force, at the onset of slip, a friction coefficient  $\mu_s(33.3$  N,  $30^\circ) = 2.0$  can here be calculated using Eq. 2.



asymmetry in  $\mu_s$  for the opposite directions  $\theta = 60^\circ$  and  $\theta = 240^\circ$ . Indeed, due to the finite size of our tested pieces, the interlocking of the chip is relatively free to unlock laterally along the  $\theta = 60^\circ$  direction, but is strongly locked by the surrounding plaster along the  $\theta = 240^\circ$  direction (see **Figure 9**).

Because the overall friction is likely to be affected by the surface wear, and because this wear is likely stress-dependent, we have performed some friction tests on  $S_m$  under various loads  $\sigma_N$ , at a given angle  $\theta = 90^\circ$ . The results are shown in **Figure 10**. At the highest tested stresses,  $\mu_s$  seems, to an extent,



stress-independent, with its mean variations lying within the measured error bars. While this result is compatible with the classical Coulomb theory [e.g., Bowden and Tabor (1951)], one can observe, over a wider range of normal stresses, a consistent decrease in the friction coefficient with a higher normal stress. It could, in part,

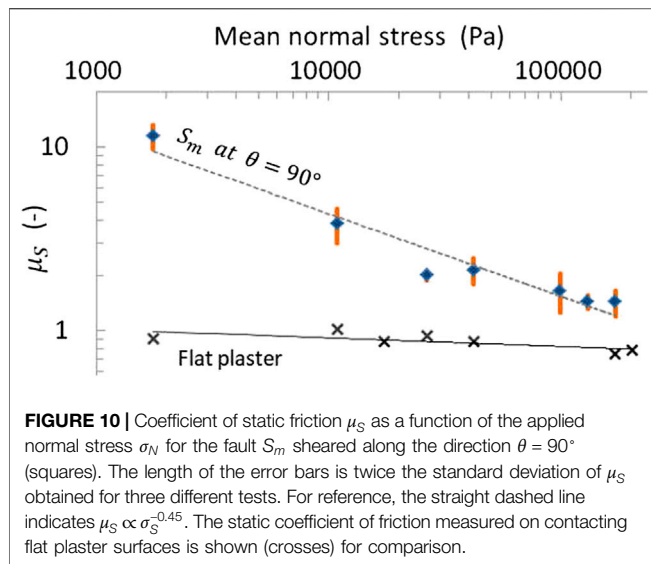


**FIGURE 10 |** Coefficient of static friction  $\mu_S$  as a function of the applied normal stress  $\sigma_N$  for the fault  $S_m$  sheared along the direction  $\theta = 90^\circ$  (squares). The length of the error bars is twice the standard deviation of  $\mu_S$  obtained for three different tests. For reference, the straight dashed line indicates  $\mu_S \propto \sigma_N^{-0.45}$ . The static coefficient of friction measured on contacting flat plaster surfaces is shown (crosses) for comparison.

emanate from some limitations in our experimental set-up. For instance, at lower  $\sigma_N$ , the internal friction of the device ( $F_c$ ) accounts for a more significant portion of the total measured tangential force, and the friction characterization could thus be less accurate. We have however run similar tests on flat plaster surfaces, showing no significant variations in  $\mu_S$  over the same stress range (see **Figure 10**). The drop in friction coefficient with  $\sigma_N$  is then likely related to the increased damage under higher normal loading (see **Figure 8**), reducing the overall shear resistance as asperities are easier to break. It might also result from the change in effective contact area with a higher load, with proportionally more pressure being borne by the surfaces parallel to the demanded motion, causing proportionally less of a resistance to slip. Such a drop of  $\mu_S$  with the normal stress has already been reported for tilted contacts [Ben-David and Fineberg (2011)], as the static coefficient of friction is not an absolute material constant [Ben-David and Fineberg (2011), Hanaor et al. (2016)].

We have therefore assessed the effect of the normal stress  $\sigma_N$  on the anisotropy of the static friction coefficient. We performed frictional tests on the four poles of  $S_m$  ( $\theta = 0^\circ, 90^\circ, 180^\circ$  and  $270^\circ$ ) at a higher load ( $\sigma_N = 171$  kPa) than the load used before (i.e.,  $\sigma_N = 10.9$  kPa, as reported in **Figure 7**). The newly measured coefficients of static friction are shown in **Figure 11**. One can notice the reduced friction anisotropy at high  $\sigma_N$ . The ratio between the maximum and the minimum value of  $\mu_S$  indeed drops from 3.1 at  $\sigma_N = 10.9$  kPa to 1.5 at  $\sigma_N = 171$  kPa. This result suggests that the frictional anisotropy of faults is smaller at depth. This concept is naturally linked with the seminal Byerlee (1978)'s law, stating that the roughness of fault planes (and the type of their constitutive rocks) has less effect on their maximum static frictional properties at larger depths.

## 5 DISCUSSION AND CONCLUSION

Here, we have shown how the multiscale anisotropy of fault plane topography leads to an anisotropy in the frictional properties.

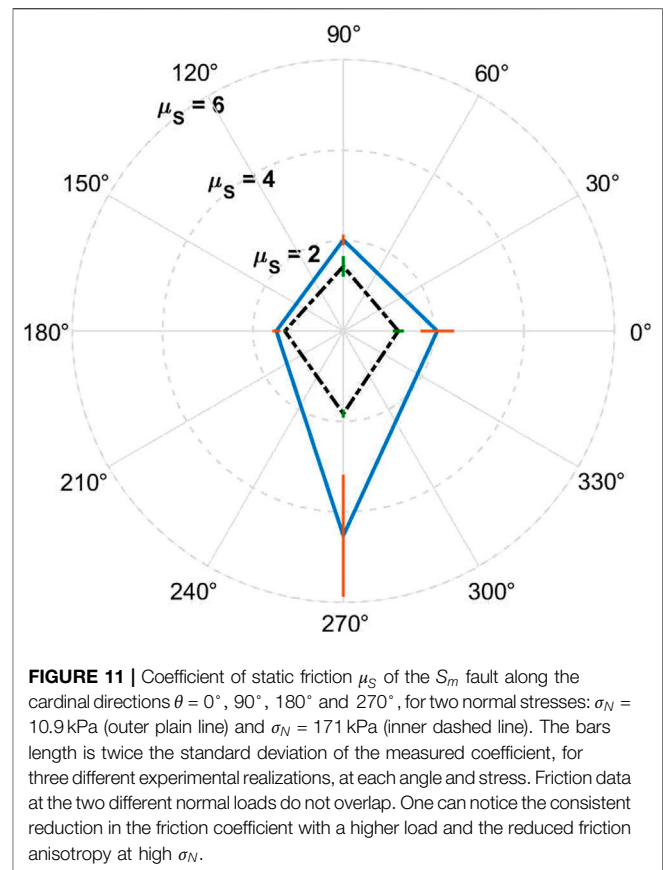


**FIGURE 11 |** Coefficient of static friction  $\mu_S$  of the  $S_m$  fault along the cardinal directions  $\theta = 0^\circ, 90^\circ, 180^\circ$  and  $270^\circ$ , for two normal stresses:  $\sigma_N = 10.9$  kPa (outer plain line) and  $\sigma_N = 171$  kPa (inner dashed line). The bars length is twice the standard deviation of the measured coefficient, for three different experimental realizations, at each angle and stress. Friction data at the two different normal loads do not overlap. One can notice the consistent reduction in the friction coefficient with a higher load and the reduced friction anisotropy at high  $\sigma_N$ .

Results confirm that seismic faults are prone to slide along some preferential orientations. The orientation that is the most likely is the one that faults have previously slid along and which has shaped some guiding grooves in their morphology. Yet, displacements following other orientations are possible. Predicting the rupture direction of the next earthquake on a fault is thus not only dependent on assessing the main regional stress. The question should rather be along which orientation a rupture criterion [e.g., Bowden and Tabor (1951)] will first be exceeded. Such a subtlety might be of little importance for mature faults for which the stress principle orientations have not changed with time, because in this case, the main stress is likely to act along the lowest coefficient of friction anyway. Yet, it could be paramount for faults under a changing geological load, where this alignment is not verified, or for immature faults, where the slip could be mainly governed by the anisotropy of early surfaces (i.e., where the slip does not coincide with the stress principal orientation, but is nonassociated). Examples of slickensides (i.e., fault planes) commonly exist with several overlapping striations orientations [e.g., Cashman and Ellis (1994)], with rake and striations oblique to the actual orientation of the fault plane [e.g., Sagy and Hamiel (2017)]. These observations indicate that the original slip direction (if assumed to initiate the following Andersonian criterion) [Célérier (2008)] does not completely determine the direction of the next episode. Earthquakes occurring along abnormal directions (i.e., not in agreement with the local stress state) have been observed [e.g.,

Satake and Kanamori (1991), Célérier (2008), Avouac et al. (2014)], and their understanding might be eased by accounting for the possible frictional anisotropy of their surfaces [Bott (1959), Pollard et al. (1993)].

Note that frictional anisotropy should not only be considered at the full fault scale, but this property may spatially vary along the fault walls. Analytical solutions demonstrate that the stress around a fault is perturbed by its roughness, and a local slip can occur much before the entire fault is under yielding conditions in a given direction [Sagy and Lyakhovskiy (2019)]. While we have here only measured the static coefficient of friction, we suggest that similar studies could be performed to characterize the anisotropy of the coefficient of dynamic friction (i.e., by analyzing the evolution of the resistance to motion, after the plaster faults start moving, as a function of the sliding orientation). Hence, not only the initial slip direction of an earthquake could be impacted by frictional anisotropy, but the complete slip trajectory [Tapia et al. (2016)]. Changes in the slip direction within single earthquake rupture events are indeed sometimes observed, notably from bent grooves on postmortem fault walls [Otsubo et al. (2013)]. We have, additionally, measured how the anisotropy in friction becomes less significant when the normal stress acting on a fault increases (i.e., with the fault depth), in general agreement with Byerlee's law [Byerlee (1978)]. Such an effect likely derives from the stress-related changes in rupture rheology and in damage type. The transition from a highly anisotropic to a relatively isotropic regime should typically occur when local stresses on the fault reach the yield strength of the material,  $\sigma_y \sim 5$  MPa in the case of plaster [Vekinis et al. (1993)]. This is about two orders of magnitude above the transition  $\sigma_N \sim 100$  kPa at which we observed a strong reduction in anisotropy (see **Figure 11**), but our computed  $\sigma_N$  is an average value which does not account for the potential strong stress concentrations at play in our faults. Considering that the strength  $\sigma_y$  of rocks [e.g., Brady et al. (1993)] is about two orders of magnitude (100 times) larger than that of plaster, fault frictional anisotropy could thus be only at play at pressures less than about  $\sigma_N \sim 100 \times 100$  kPa = 10 MPa. This would correspond to the shallowest faults, at depths less than  $\sigma_N/(g\rho) \sim 500$  m, where  $\rho$  is the volumetric mass of rocks ( $\sim 2000$  kg m<sup>-3</sup>) and  $g$  the gravity acceleration. Some care should however be taken when deriving such a conclusion by analyzing resized samples as ours (40 mm diameter samples representing meter or millimeter topographies), as the way matter breaks is length-scale-dependent [e.g., Brodsky et al. (2016)]. Note also that other fault geometries than the one we have here studied may induce lesser stress concentration, so that a significant damage only occurs at a mean stress level directly comparable to the yield stress  $\sigma_y$  of rocks. Thus, the possibility of frictional anisotropy should not be overlooked when studying fault buried up to  $\sigma_y/(g\rho) \sim 50$  km. The heterogeneity of fault planes, and thus the anisotropy in this heterogeneity, may also still play a role under high stress, as roughness does not only encourage local yield, but also helps to suppress large slip events on moving faults [Bruhat et al. (2019)].

Additionally to the assessment of the stability of (at least) shallow seismic faults, the characterization of the frictional

anisotropy of rock surfaces may be of importance in geotechnical engineering, for instance, for the stability of tunnels and foundations. There, the intrinsic strength anisotropy of foliated rocks is well-studied [Shea and Kronenberg (1993), Rawling et al. (2002)]. Our work shows how one can also characterize the mechanical anisotropy of rough rock contacts, for instance, along joints [Barton and Choubey (1977), Seidel and Haberfeld (1995), Grasselli and Egger (2003), Li et al. (2020)] and fractures [Ponson et al. (2006a), Ponson et al. (2000b)] between or inside rock formations.

A main point of this manuscript is, finally, to illustrate how the 3D-printing technology can help with new experimental designs in Earth Sciences, and this technology is getting a growing attention from the community [Wang L. et al. (2017), Squelch (2017), Wang et al. (2018), Feng et al. (2019), Braun et al. (2020)], including the study of the frictional properties of 3D-printed fault analogs [Braun et al. (2020)]. A direct continuation of the present work, for instance, could be to 3D-print and to test some faults surfaces beforehand filtered with various band-pass filters, in order to understand how the various wavelengths of the topography contribute to the global static friction coefficient, to the dynamical friction coefficient and to analyze the spatial distribution of the fault wear produced under various stresses and amounts of slip.

## DATA AVAILABILITY STATEMENT

The original contributions presented in the study are included in the article/**Supplementary Materials**; further inquiries can be directed to the corresponding authors.

## AUTHOR CONTRIBUTIONS

RT proposed the guidelines of this work, AS built the test machine and, with TV-D, printed the faults and performed the friction experiments. FR advised on the mechanics of seismic faults. TV-D wrote the first version of this manuscript and all authors contributed to the writing of its final version.

## FUNDING

We acknowledge the support of the University of Strasbourg, of the IRP France–Norway D-FFRACT, and of SFF Porelab (project number 262644 of the Research Council of Norway). Readers are welcome to comment and correspondence should be addressed to tom.vincent-dospital@fys.uio.no. or renaud.toussaint@unistra.fr.

## ACKNOWLEDGMENTS

We are grateful for the early experimental explorations performed by Marine-Sophie Jacob, Céline Fliedner, Aldo

Mellado Aguilar, Gaëtan Leca, and Laifa Rahmi, students from the EOST/IPGS faculty at the University of Strasbourg. We also thank Amir Sagy from the Geological Survey of Israel for fruitful discussions. We thank the Strasbourg AV.Lab association for letting us use their 3D printer.

## REFERENCES

- Allam, A. A., Kroll, K. A., Milliner, C. W. D., and Richards-Dinger, K. B. (2019). Effects of fault roughness on coseismic slip and earthquake locations. *J. Geophys. Res. Solid Earth* 124 (11), 11336–11349. doi:10.1029/2018JB016216
- Ando, R., Takeda, N., and Yamashita, T. (2012). Propagation dynamics of seismic and aseismic slip governed by fault heterogeneity and Newtonian rheology. *J. Geophys. Res.* 117 (B11), 11308. doi:10.1029/2012JB009532
- Aochi, H., and Ide, S. (2009). Complexity in earthquake sequences controlled by multiscale heterogeneity in fault fracture energy. *J. Geophys. Res.* 114 (B3). doi:10.1029/2008JB006034
- Avouac, J.-P., Ayoub, F., Wei, S., Ampuero, J.-P., Meng, L., Leprince, S., et al. (2014). The 2013, Mw 7.7 Balochistan earthquake, energetic strike-slip reactivation of a thrust fault. *Earth Planet. Sci. Lett.* 391, 128–134. doi:10.1016/j.epsl.2014.01.036
- Barton, N., and Choubey, V. (1977). The shear strength of rock joints in theory and practice. *Rock Mech.* 10, 1–54. doi:10.1007/BF01261801
- Ben-David, O., and Fineberg, J. (2011). Static friction coefficient is not a material constant. *Phys. Rev. Lett.* 106, 254301. doi:10.1103/PhysRevLett.106.254301
- Blakely, R. J., Wells, R. E., Weaver, C. S., and Johnson, S. Y. (2002). Location, structure, and seismicity of the Seattle fault zone, Washington: evidence from aeromagnetic anomalies, geologic mapping, and seismic-reflection data. *GSA Bull.* 114 (2), 169–177. doi:10.1130/0016-7606(2002)114;0169:LSASOT;2.0.CO;2
- Blanpied, M. L., Lockner, D. A., and Byerlee, J. D. (1992). An earthquake mechanism based on rapid sealing of faults. *Nature* 358, 574–576. doi:10.1038/358574a0
- Bott, M. H. P. (1959). The mechanics of oblique slip faulting. *Geol. Mag.* 96 (2), 109–117. doi:10.1017/S0016756800059987
- Bouchon, M., Karabulut, H., Bouin, M.-P., Schmittbuhl, J., Vallée, M., Archuleta, R., et al. (2010). Faulting characteristics of supershear earthquakes. *Tectonophysics* 493 (3), 244–253. doi:10.1016/j.tecto.2010.06.011
- Bowden, F. P., and Tabor, D. (1951). The friction and lubrication of solids. *Am. J. Phys.* 19 (7), 428–429. doi:10.1119/1.1933017
- Brady, B. T., Duvall, W. I., and Horino, F. G. (1993). An experimental determination of the true uniaxial stress-strain behavior of brittle rock. *Rock Mech.* 5, 107–120. doi:10.1007/BF01240161
- Braun, P., Tzortzopoulos, G., and Stefanou, I. (2020). Design of sand-based, 3d-printed analogue faults with controlled frictional properties. *J. Geophys. Res.* [preprint]. doi:10.1002/essoar.10503633.1
- Brodsky, E. E., Kirkpatrick, J. D., and Candela, T. (2016). Constraints from fault roughness on the scale-dependent strength of rocks. *Geology* 44 (1), 19–22. doi:10.1130/G37206.1
- Brown, S. R., and Scholz, C. H. (1985). Broad bandwidth study of the topography of natural rock surfaces. *J. Geophys. Res.* 90 (B14), 12575–12582. doi:10.1029/JB090iB14p12575
- Bruhat, L., Klinger, Y., Vallage, A., and Dunham, E. M. (2019). Influence of fault roughness on surface displacement: from numerical simulations to coseismic slip distributions. *Geophys. J. Int.* 220 (3), 1857–1877. doi:10.1093/gji/ggz545
- Byerlee, J. (1978). Friction of rocks. *Pure Appl. Geophys.* 116 (4), 615–626. doi:10.1007/BF00876528
- Campione, M., and Capitani, G. C. (2013). Subduction-zone earthquake complexity related to frictional anisotropy in antigorite. *Nat. Geosci.* 6, 847–851. doi:10.1038/ngeo1905
- Candela, T., and Brodsky, E. E. (2016). The minimum scale of grooving on faults. *Geology* 44 (8), 603–606. doi:10.1130/G37934.1
- Candela, T., and Renard, F. (2012). Fault morphology database. Available at: <https://www.isterre.fr/french/recherche-observation/equipes/mecanique-des-failles/moyens-et-outils/article/donnees.html> (Accessed 2020).
- Candela, T., Renard, F., Schmittbuhl, J., Bouchon, M., and Brodsky, E. E. (2011). Fault slip distribution and fault roughness. *Geophys. J. Int.* 187 (2), 959–968. doi:10.1111/j.1365-246X.2011.05189.x
- Candela, T., Renard, F., Klinger, Y., Mair, K., Schmittbuhl, J., and Brodsky, E. E. (2012). Roughness of fault surfaces over nine decades of length scales. *J. Geophys. Res.* 117 (B8), B08409. doi:10.1029/2011JB009041
- Carbone, G., Lorenz, B., Persson, B. N. J., and Wohlers, A. (2009). Contact mechanics and rubber friction for randomly rough surfaces with anisotropic statistical properties. *Eur. Phys. J. J.* 29 (3), 275–284. doi:10.1140/epje/i2009-10484-8
- Cashman, P. H., and Ellis, M. A. (1994). Fault interaction may generate multiple slip vectors on a single fault surface. *Geology* 22 (12), 1123–1126. doi:10.1130/0091-7613(1994)022;1123:FIMGMS;2.3.CO;2
- Célérier, B. (2008). Seeking Anderson's faulting in seismicity: a centennial celebration. *Rev. Geophys.* 46 (4). doi:10.1029/2007RG000240
- Cochran, E. S., Vidale, J. E., and Li, Y.-G. (2003). Near-fault anisotropy following the Hector Mine earthquake. *J. Geophys. Res.* 108 (B9) 2436. doi:10.1029/2002JB002352
- Di Toro, G., Han, R., Hirose, T., De Paola, N., Nielsen, S., Mizoguchi, K., et al. (2011). Fault lubrication during earthquakes. *Nature* 471, 494–498. doi:10.1038/nature09838
- Edwards, J. H., Kluesner, J. W., Silver, E. A., Brodsky, E. E., Brothers, D. S., Bangs, N. L., et al. (2018). Corrugated megathrust revealed offshore from Costa Rica. *Nat. Geosci.* 11, 197–202. doi:10.1038/s41561-018-0061-4
- Engelder, J. T. (1974). Microscopic wear grooves on slickensides: indicators of paleoseismicity. *J. Geophys. Res.* 79 (29), 4387–4392. doi:10.1029/JB079i029p04387
- Evans, R. (1984). Anisotropy: a pervasive feature of fault zones? *Geophys. J. Int.* 76 (1), 157–163. doi:10.1111/j.1365-246X.1984.tb05031.x
- Feng, X.-T., Gong, Y.-H., Zhou, Y.-Y., Li, Z.-W., and Liu, X.-F. (2019). The 3D-printing technology of geological models using rock-like materials. *Rock Mech. Rock Eng.* 52, 2261–2277. doi:10.1007/s00603-018-1703-y
- Fessler, G., Sadeghi, A., Glatzel, T., Goedecker, S., and Meyer, E. (2019). Atomic friction: anisotropy and asymmetry effects. *Tribol. Lett.* 67 (2), 59. doi:10.1007/s11249-019-1172-9
- Filippov, A., and Gorb, S. N. (2013). Frictional-anisotropy-based systems in biology: structural diversity and numerical model. *Sci. Rep.* 3, 1240. doi:10.1038/srep01240
- Filippov, A. E., Westhoff, G., Kovalev, A., and Gorb, S. N. (2018). Numerical model of the slithering snake locomotion based on the friction anisotropy of the ventral skin. *Tribol. Lett.* 66. doi:10.1007/s11249-018-1072-4
- Gong, H., Zhu, P., Si, L., Zhang, X., and Xie, G. (2018). “M-shape” nanoscale friction anisotropy of phosphorene. *Comput. Mater. Sci.* 150, 364–368. doi:10.1016/j.commatsci.2018.04.013
- Grasselli, G., and Egger, P. (2003). Constitutive law for the shear strength of rock joints based on three-dimensional surface parameters. *Int. J. Rock Mech. Mining Sci.* 40 (1), 25–40. doi:10.1016/S1365-1609(02)00101-6
- Hanaor, D. A. H., Gan, Y., and Einav, I. (2016). Static friction at fractal interfaces. *Tribol. Int.* 93, 229–238. doi:10.1016/j.triboint.2015.09.016
- Jin, K., Tian, Y., Erickson, J. S., Puthoff, J., Autumn, K., and Pesika, N. S. (2012). Design and fabrication of gecko-inspired adhesives. *Langmuir* 28, 5737–5742. doi:10.1021/la204040p
- Kim, Y.-S., Peacock, D. C. P., and Sanderson, D. J. (2004). Fault damage zones. *J. Struct. Geology* 26 (3), 503–517. doi:10.1016/j.jsg.2003.08.002
- Li, Z., Peng, Z., Ben-Zion, Y., and Vernon, F. L. (2015). Spatial variations of shear wave anisotropy near the San Jacinto fault zone in Southern California. *J. Geophys. Res. Solid Earth* 120 (12), 8334–8347. doi:10.1002/2015JB012483
- Li, Y., Tang, C. A., Li, D., and Wu, C. (2020). A new Shear strength criterion of three-dimensional rock joints. *Rock Mech. Rock Eng.* 53, 1477–1483. doi:10.1007/s00603-019-01976-5

## SUPPLEMENTARY MATERIAL

The Supplementary Material for this article can be found online at: <https://www.frontiersin.org/articles/10.3389/feart.2021.627823/full#supplementary-material>

- Massonnet, D., Rossi, M., Carmona, C., Adragna, F., Peltzer, G., Feigl, K., et al. (1993). The displacement field of the Landers earthquake mapped by radar interferometry. *Nature* 364, 138–142. doi:10.1038/364138a0
- Mitchell, T. M., and Faulkner, D. R. (2008). Experimental measurements of permeability evolution during triaxial compression of initially intact crystalline rocks and implications for fluid flow in fault zones. *J. Geophys. Res.* 113 (B11). doi:10.1029/2008JB005588
- Otsubo, M., Shigematsu, N., Imanishi, K., Ando, R., Takahashi, M., and Azuma, T. (2013). Temporal slip change based on curved slickenlines on fault scarps along Itozawa fault caused by 2011 Iwaki earthquake, Northeast Japan. *Tectonophysics* 608, 970–979. doi:10.1016/j.tecto.2013.07.022
- Peacock, D. C. P., and Sanderson, D. J. (1992). Effects of layering and anisotropy on fault geometry. *J. Geol. Soc.* 149 (5), 793–802. doi:10.1144/gsjgs.149.5.0793
- Pechmann, J. C., and Kanamori, H. (1982). Waveforms and spectra of preshocks and aftershocks of the 1979 imperial valley, california, earthquake: evidence for fault heterogeneity? *J. Geophys. Res.* 87 (B13), 10579–10597. doi:10.1029/JB087B13p10579
- Pionnier, N., Vera, J., Contraires, E., Benayoun, S., Berger, R., and Valette, S. (2018). The effect of the orientation and the height of periodic sub-micrometric texturing on dropwise condensation. *J. Colloid Interf. Sci.* 526, 184–193. doi:10.1016/j.jcis.2018.04.043
- Pollard, D. D., Saltzer, S. D., and Rubin, A. M. (1993). Stress inversion methods: are they based on faulty assumptions? *J. Struct. Geol.* 15 (8), 1045–1054. doi:10.1016/0191-8141(93)90176-B
- Ponson, L., Bonamy, D., Auradou, H., Mourrot, G., Morel, S., Bouchaud, E., et al. (2006a). Anisotropic self-affine properties of experimental fracture surfaces. *Int. J. Fract.* 140, 27–37. doi:10.1007/s10704-005-3059-z
- Ponson, L., Bonamy, D., and Bouchaud, E. (2006b). Two-dimensional scaling properties of experimental fracture surfaces. *Phys. Rev. Lett.* 96, 035506. doi:10.1103/PhysRevLett.96.035506
- Queener, C. A., Smith, T. C., and Mitchell, W. L. (1965). Transient wear of machine parts. *Wear* 8 (5), 391–400. doi:10.1016/0043-1648(65)90170-5
- Quinsat, Y., Lartigue, C., Brown, C. A., and Hattali, L. (2018). Characterization of surface topography of 3d printed parts by multi-scale analysis. *Int. J. Interact. Des. Manuf.* 12 (3), 1007–1014. doi:10.1007/s12008-017-0433-9
- Rawling, G. C., Baud, P., and Wong, T.-F. (2002). Dilatancy, brittle strength, and anisotropy of foliated rocks: experimental deformation and micromechanical modeling. *J. Geophys. Res.* 107 (B10), 8–1. doi:10.1029/2001JB000472
- Rempel, A. W., and Rice, J. R. (2006). Thermal pressurization and onset of melting in fault zones. *J. Geophys. Res.* 111 (B9). doi:10.1029/2006JB004314
- Renard, V., Hekinian, R., Francheteau, J., Ballard, R. D., and Backer, H. (1985). Submersible observations at the axis of the ultra-fast-spreading East Pacific rise (17°30' to 21°30'S). *Earth Planet. Sci. Lett.* 75 (4), 339–353. doi:10.1016/0012-821X(85)90178-5
- Renard, F., Voisin, C., Marsan, D., and Schmittbuhl, J. (2006). High resolution 3d laser scanner measurements of a strike-slip fault quantify its morphological anisotropy at all scales. *Geophys. Res. Lett.* 33 (4). doi:10.1029/2005GL025038
- Renard, F. (2020). Data From: Frictional anisotropy of 3D-printed fault surfaces. Fault roughness data. <https://dx.doi.org/10.3389/feart.2021.627823>.
- Rice, J. R., and Ben-Zion, Y. (1996). Slip complexity in earthquake fault models. *Proc. Natl. Acad. Sci.* 93 (9), 3811–3818. doi:10.1073/pnas.93.9.3811
- Roth-Nebelsick, A., Ebner, M., Miranda, T., Gottschalk, V., Voigt, D., Gorb, S., et al. (2012). Leaf surface structures enable the endemic Namib desert grass *Stipagrostis sabulicola* to irrigate itself with fog water. *J. R. Soc. Interf.* 9 (73), 1965–1974. doi:10.1098/rsif.2011.0847
- Sagy, A., and Hamiel, Y. (2017). Three-dimensional structure and evolution of an asymmetric pull-apart basin. *Int. J. Earth Sci. (Geol. Rundsch)* 106, 1619–1630. doi:10.1007/s00531-016-1374-4
- Sagy, A., and Lyakhovskiy, V. (2019). Stress patterns and failure around rough interlocked fault surface. *J. Geophys. Res. Solid Earth* 124 (7), 7138–7154. doi:10.1029/2018JB017006
- Satake, K., and Kanamori, H. (1991). Abnormal tsunamis caused by the June 13, 1984, Torishima, Japan, earthquake. *J. Geophys. Res.* 96 (B12), 19933–19939. doi:10.1029/91JB01903
- Sauter FH-S. (2018). Technical information. Technical report, Sauter. Available at: <https://dokkern-sohn.com/manuals/files/English/FH-S-BA-e-1819.pdf> (Accessed 2020).
- Seidel, J. P., and Haberfield, C. M. (1995). The application of energy principles to the determination of the sliding resistance of rock joints. *Rock Mech. Rock Eng.* 28, 211–226. doi:10.1007/BF01020227
- Shea, W. T., and Kronenberg, A. K. (1993). Strength and anisotropy of foliated rocks with varied mica contents. *J. Struct. Geol.* 15 (9), 1097–1121. doi:10.1016/0191-8141(93)90158-7
- Squelch, A. (2017). 3D printing rocks for geo-educational, technical, and hobbyist pursuits. *Geosphere* 14 (1), 360–366. doi:10.1130/GES01364.1
- Stupkiewicz, S., Lewandowski, M. J., and Lengiewicz, J. (2014). Micromechanical analysis of friction anisotropy in rough elastic contacts. *Int. J. Sol. Struct.* 51 (23), 3931–3943. doi:10.1016/j.ijsolstr.2014.07.013
- Tapia, F., Tourneau, D. L., and Géminard, J.-C. (2016). Anisotropic friction: assessment of force components and resulting trajectories. *EPJ Techn. Instrum.* 3, 1. doi:10.1140/epjti/s40485-016-0029-y
- Tesei, T., Colletini, C., Barchi, M. R., Carpenter, B. M., and Di Stefano, G. (2014). Heterogeneous strength and fault zone complexity of carbonate-bearing thrusts with possible implications for seismicity. *Earth Planet. Sci. Lett.* 408, 307–318. doi:10.1016/j.epsl.2014.10.021
- Tiwari, A., Dorogin, L., Steenwyk, B., Warhadpande, A., Motamedi, M., Fortunato, G., et al. (2016). Rubber friction directional asymmetry. *Epl* 116 (6), 66002. doi:10.1209/0295-5075/116/66002
- Ultimaker2 Extended+. (2015). Technical information. Technical report, Ultimaker. Available at: <https://ultimaker.com/download/7386/UserManual-UM2Extended-v2.1.pdf> (Accessed 2020).
- Vadacca, L., Colciago, C. M., Micheletti, S., and Scotti, A. (2018). Effects of the anisotropy of the fault zone permeability on the timing of triggered earthquakes: insights from 3d-coupled fluid flow and geomechanical deformation modeling. *Pure Appl. Geophys.* 175 (12), 4131–4144. doi:10.1007/s00024-018-1936-4
- Vekinis, G., Ashby, M. F., and Beaumont, P. W. R. (1993). Plaster of Paris as a model material for brittle porous solids. *J. Mater. Sci.* 28, 3221–3227. doi:10.1007/BF00354239
- Wang, W., and Scholz, C. H. (1994). Wear processes during frictional sliding of rock: a theoretical and experimental study. *J. Geophys. Res.* 99 (B4), 6789–6799. doi:10.1029/93JB02875
- Wang, F., Wang, L., Wu, H., Pang, J., Gu, D., and Li, S. (2017a). A lotus-leaf-like sio2 superhydrophobic bamboo surface based on soft lithography. *Colloids Surf. A Physicochem. Eng. Asp.* 520, 834–840. doi:10.1016/j.colsurfa.2017.02.043
- Wang, L., Ju, Y., Xie, H., Ma, G., Mao, L., and He, K. (2017b). The mechanical and photoelastic properties of 3D printable stress-visualized materials. *Sci. Rep.* 7. doi:10.1038/s41598-017-11433-4
- Wang, J., Stewart, R. R., and Dyaur, N. I. (2018). Seismic response analysis of a 3D-printed dual-porosity physical model: Marine case. *SEG*, 301–305. doi:10.1190/segam2018-2997200.1
- Wibberley, C. A. J., Yielding, G., and Di Toro, G. (2008). Recent advances in the understanding of fault zone internal structure: a review. *Geol. Soc. Lond. Spec. Publ.* 299 (1), 5–33. doi:10.1144/SP299.2
- Yu, C., and Wang, Q. J. (2012). Friction anisotropy with respect to topographic orientation. *Sci. Rep.* 2, 988. doi:10.1038/srep00988
- Zheng, Y., Gao, X., and Jiang, L. (2007). Directional adhesion of superhydrophobic butterfly wings. *Soft Matter* 3, 178–182. doi:10.1039/B612667G

**Conflict of Interest:** The authors declare that the research was conducted in the absence of any commercial or financial relationships that could be construed as a potential conflict of interest.

Copyright © 2021 Vincent-Dospital, Steyer, Renard and Toussaint. This is an open-access article distributed under the terms of the Creative Commons Attribution License (CC BY). The use, distribution or reproduction in other forums is permitted, provided the original author(s) and the copyright owner(s) are credited and that the original publication in this journal is cited, in accordance with accepted academic practice. No use, distribution or reproduction is permitted which does not comply with these terms.